

Improved Quadcopter Disturbance Rejection Using Added Angular Momentum

Nathan Bucki and Mark W. Mueller

Abstract—This paper presents a novel quadcopter design with an added momentum wheel for enhanced stability. The novel vehicle has improved torque disturbance rejection capabilities compared to a standard quadcopter. An analysis of the vehicle dynamics shows that the effect of torque disturbances decreases monotonically with increasing angular momentum of the momentum wheel. A framework for choosing the mass moment of inertia and speed of the momentum wheel is given based on an upper bound on the allowable energy stored in the wheel. Theoretical results are experimentally validated by comparing responses to torque impulses applied to the vehicle with and without the momentum wheel spinning.

I. INTRODUCTION

In recent years, quadcopters have been widely used for a variety of applications such as aerial imaging [1], environmental monitoring [2], building inspection [3], and search and rescue [4]. However, the operation of these vehicles is currently limited in environments with major disturbances. While several control schemes have been developed that aim to reduce the effect of disturbances (such as the switching MPC attitude controller presented in [5] and the disturbance accommodation controller presented in [6]), the performance of the vehicle is inherently limited by its dynamics and by the available range of control inputs. Thus, any increases in performance beyond the capabilities of a control algorithm necessarily require changes to the vehicle design.

One such change is to include a large source of angular momentum on the vehicle in the form of a momentum wheel. A realization of this concept is shown in Figure 1. The contribution of the momentum wheel to the dynamics of the vehicle can be scaled mid-flight by changing the speed at which it spins, allowing for the dynamics of the vehicle to be changed without a proportional increase in mass. The additional angular momentum of the vehicle allows for an improved rejection of torque disturbances, enhancing the ability of the vehicle to fly in environments with high wind shear or flying debris (e.g. tornadoes, hail storms, etc.).

The additional angular momentum results in dynamics similar to those of dual-spin spacecraft, which are defined by the use of two bodies rotating about a shared spin axis to maintain a desired attitude. The attitude stability criteria for dual spin spacecraft are presented in [7].

Other unconventional quadcopter designs capable of changing the dynamics of the vehicle mid-flight include a quadcopter with tilting propellers as presented in [8] and a quadcopter capable of changing the length and orientation of

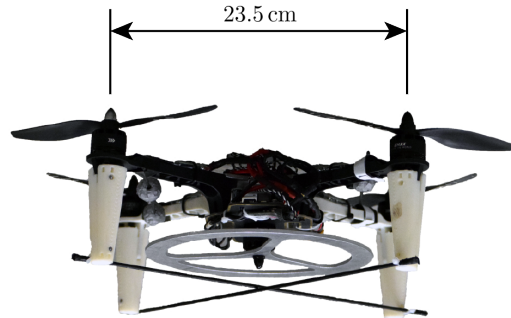


Fig. 1. Quadcopter with added momentum wheel, shown from below. The momentum wheel is driven by a speed-controlled motor mounted underneath the vehicle.

its arms as presented in [9]. Both of these vehicles increase the number of available control inputs to the system, resulting in a vehicle that is potentially more maneuverable/versatile than a standard quadcopter. Additionally, the dynamics of rotating flying machines has been investigated in [10] and [11], showing vehicles with significant angular momentum are able to be controlled with fewer actuators. In contrast to these designs, we focus specifically on improving the disturbance rejection of the vehicle.

This paper is organized as follows: Section II derives the dynamics of the vehicle, Section III details the controller architecture, Section IV describes how the momentum wheel parameters are chosen, and Section V presents experimental data.

II. DERIVATION OF SYSTEM DYNAMICS

In this section we present the derivation of the full vehicle dynamics as well as a linearized version of the rotational dynamics.

A. Notation

Non-bold symbols such as m represent scalars, lowercase bold symbols such as \mathbf{g} represent first order tensors (vectors), and uppercase bold symbols such as \mathbf{J} represent second order tensors (matrices). The short-hand notation (x, y, z) represents a column vector. Subscripts such as m_B represent the body to which the scalar/tensor is related, and superscripts such as \mathbf{g}^E represent the frame in which the tensor is expressed. The inertial frame is notated with E and the body-fixed frame with B .

B. System Dynamics

Figure 2 shows a model of the augmented quadcopter. The mass and mass moment of inertia of the quadcopter are

The authors are with the High Performance Robotics Lab, University of California, Berkeley, CA 94703, USA. {nathan.bucki, mwm}@berkeley.edu

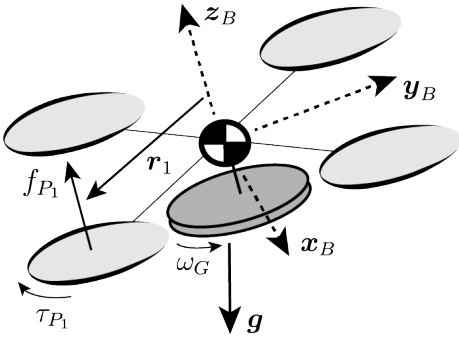


Fig. 2. Model of quadcopter with added momentum wheel. The momentum wheel rotates about z_B with angular velocity ω_G . Each propeller produces thrust force f_{P_i} and reaction torque τ_{P_i} about the propeller's axis of rotation at a distance r_i from the center of mass.

denoted m_B and \mathbf{J}_B , and the mass and mass moment of inertia of the momentum wheel are denoted m_G and \mathbf{J}_G . The momentum wheel spins about z_B with angular velocity $\omega_G^B = (0, 0, \omega_G)$ relative to the body-fixed frame. The total vehicle mass is written as $m_\Sigma = m_B + m_G$, and the total vehicle inertia is written as $\mathbf{J}_\Sigma^B = \mathbf{J}_B^B + \mathbf{J}_G^B$. Note that \mathbf{J}_G^B is constant when expressed in the body-fixed frame due to the axial symmetry of the momentum wheel about its axis of rotation.

Each propeller produces thrust force f_{P_i} in the direction of z_B at a displacement r_i from the vehicle center of mass. The reaction torque produced by a given propeller is assumed to be linearly related to the thrust force by $\tau_{P_i} = \kappa_i f_{P_i}$, where the magnitude and sign of κ_i are determined by the geometry and rotation direction of propeller i [12].

The attitude of the quadcopter is written as yaw, pitch, and roll (notated ψ, θ, ϕ), and the angular velocity of the quadcopter is given as $\omega_B^B = (p, q, r)$ where p, q and r are the body rates of the vehicle about the x_B, y_B , and z_B axes respectively. The position of the quadcopter relative to a fixed point in the inertial frame is written as $d_B^E = (x, y, z)$.

The translational dynamics of the system are derived using Newton's second law for rigid bodies, where the external forces are taken to be the four thrust forces and gravity [13]. The translational dynamics are expressed in the inertial frame E .

$$m_\Sigma \ddot{d}_B^E = m_\Sigma g^E + z_B^E \sum_{i=1}^4 f_{P_i} \quad (1)$$

The rotational dynamics are derived using Euler's law for clustered bodies with a fixed center of mass [13], and are expressed in the body-fixed frame. The skew-symmetric matrix form of the cross product is written as $S(\mathbf{a})$ such that $S(\mathbf{a})\mathbf{b} = \mathbf{a} \times \mathbf{b}$. The disturbance torque is written in the body-fixed frame as τ_v^B .

$$\mathbf{J}_\Sigma^B \dot{\omega}_B^B + \mathbf{J}_G^B \dot{\omega}_G^B + S(\omega_B^B) \left(\mathbf{J}_\Sigma^B \omega_B^B + \mathbf{J}_G^B \omega_G^B \right) = \sum_{i=1}^4 \left(S(r_i^B) z_B^B f_{P_i} + z_B^B \tau_{P_i} \right) + \tau_v^B \quad (2)$$

C. Linearized Rotational Dynamics

Although the momentum wheel increases the total mass of the vehicle, it mainly affects the dynamics of the system through its angular momentum. Thus, we choose to analyze how the rotational dynamics in (2) are affected by the angular momentum provided by the wheel. The rotational dynamics additionally determine the thrust direction of the quadcopter, which dominates the translational acceleration of the vehicle. Here we present the linearized rotational dynamics as background for the following controller synthesis and system analysis.

In linearizing the rotational dynamics we assume that x_B, y_B , and z_B are principal axes of inertia of both the body and the wheel. The principal mass moments of inertia in the x_B, y_B , and z_B directions are then denoted $J_{B,xx}, J_{B,yy}$, and $J_{B,zz}$ respectively for the quadcopter body and $J_{G,xx}, J_{G,yy}$, and $J_{G,zz}$ for the momentum wheel. We also assume $J_{\Sigma,xx} = J_{\Sigma,yy}$ because the quadcopter is symmetric in the x_B and y_B directions, and assume ω_G^B to be constant because the speed of the momentum wheel is controlled by a high bandwidth speed controller.

The linearized rotational dynamics are given in the form $\dot{x} = Ax + B_1 \tau_v^B + B_2 \tau_u^B$. Here we choose the states to be the attitude and body rates of the vehicle, $x = (\phi, \theta, \psi, p, q, r)$ and the control inputs to be the body torques produced by the propellers, $\tau_u^B = \sum_{i=1}^4 (S(r_i^B) z_B^B f_{P_i} + z_B^B \tau_{P_i})$. Let I represent the identity matrix.

$$A = \begin{bmatrix} 0 & I \\ 0 & A_1 \end{bmatrix}, \quad A_1 = \begin{bmatrix} 0 & -\frac{J_{G,zz}\omega_G}{J_{\Sigma,xx}} & 0 \\ \frac{J_{G,zz}\omega_G}{J_{\Sigma,yy}} & 0 & 0 \\ 0 & 0 & 0 \end{bmatrix} \\ B_1 = B_2 = \begin{bmatrix} 0 \\ (\mathbf{J}_\Sigma^B)^{-1} \end{bmatrix} \quad (3)$$

III. CONTROL ALGORITHM

The quadcopter is controlled using a cascaded control design as shown in Figure 3. The position controller computes the desired total thrust and thrust direction from the current position and velocity of the quadcopter, and the attitude controller computes the desired body torques required to track the desired thrust direction and desired yaw angle. Finally, the thrust forces of each propeller necessary to generate the desired body torques and total desired thrust are computed.

A. Position Control

The position controller is designed such that the position error behaves as a second order system with damping ratio ζ_p and natural frequency ω_p . The desired acceleration $\ddot{d}_{B,d}^E$ is computed from the desired position and velocity of the quadcopter, $\dot{d}_{B,d}^E$ and $d_{B,d}^E$. The desired thrust and thrust direction, f_{cmd} and $z_{B,d}^E$, are then computed from the desired acceleration. All quantities are expressed in the inertial

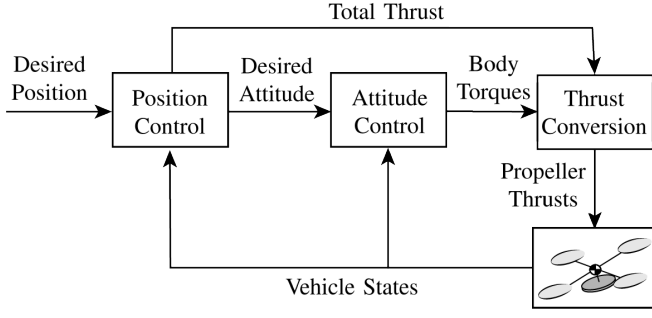


Fig. 3. Quadcopter controller architecture. An LQR attitude controller is cascaded with a position controller in order to produce desired body torques, which are then converted into propeller thrust forces. Position and orientation feedback is provided by a motion capture system, and angular velocity feedback is provided by an onboard rate gyroscope.

frame.

$$\ddot{\mathbf{d}}_{B,d}^E = 2\zeta_p\omega_p(\dot{\mathbf{d}}_{B,d}^E - \dot{\mathbf{d}}_B^E) + \omega_p^2(\mathbf{d}_{B,d}^E - \mathbf{d}_B^E) + \mathbf{g}^E \quad (4)$$

$$f_{cmd} = \|\ddot{\mathbf{d}}_{B,d}^E\|_2, \quad \mathbf{z}_{B,d}^E = \frac{\ddot{\mathbf{d}}_{B,d}^E}{\|\ddot{\mathbf{d}}_{B,d}^E\|_2} \quad (5)$$

B. Attitude Control

Let the Euler angles $(\phi_e, \theta_e, \psi_e)$ represent the rotation from the current attitude to the desired attitude, which is defined by the desired thrust direction $\mathbf{z}_{B,d}$ and the desired yaw angle. The angular velocity error is defined as $\boldsymbol{\omega}_e = \boldsymbol{\omega}_B - \boldsymbol{\omega}_{B,d}$, where $\boldsymbol{\omega}_{B,d}$ is the desired angular velocity of the quadcopter. Thus, the state vector for the linearized system defined in (3) is defined as $x = (\phi_e, \theta_e, \psi_e, \omega_{e,x}^B, \omega_{e,y}^B, \omega_{e,z}^B)$.

The optimal infinite-time LQR attitude state feedback controller $\boldsymbol{\tau}_u^B = -Kx$ is computed using the state and input quadratic cost matrices defined below. The Q and R matrices are chosen such that roll and pitch are penalized equally because of the symmetry of the vehicle. The body torques about \mathbf{x}_B and \mathbf{y}_B are penalized equally for the same reason. We choose not to explicitly penalize the angular velocity of the vehicle.

$$Q = \text{diag}(q_{xy}, q_{xy}, q_z, 0, 0, 0) \quad (6)$$

$$R = \text{diag}(r_{xy}, r_{xy}, r_z)$$

The state feedback gain that minimizes the infinite-time LQR cost function is $K = R^{-1}B_2^T P$, where P is the solution to the continuous time algebraic Riccati equation, $A^T P + PA - PB_2 R^{-1} B_2^T P = -Q$ [14]. By leveraging the fact that ψ_e and $\omega_{e,z}^B$ (yaw error and yaw rate error) are decoupled from the rest of the linearized system, we are able

to analytically solve for K in terms of the system parameters:

$$K = \begin{bmatrix} \alpha & \beta & 0 & \gamma & 0 & 0 \\ -\beta & \alpha & 0 & 0 & \gamma & 0 \\ 0 & 0 & \eta & 0 & 0 & \nu \end{bmatrix}$$

$$L = J_{G,zz}\omega_G, \quad H = \sqrt{16\frac{q_{xy}}{r_{xy}}J_{\Sigma,xx}^2 + L^4 - L^2} \quad (7)$$

$$\alpha = \frac{H}{4J_{\Sigma,xx}}, \quad \beta = \frac{L\sqrt{2H}}{4J_{\Sigma,xx}}, \quad \gamma = \frac{\sqrt{2H}}{2}$$

$$\eta = \sqrt{\frac{q_z}{r_z}}, \quad \nu = \sqrt{2J_{\Sigma,zz}\sqrt{\frac{q_z}{r_z}}}$$

The analytic solution for K allows the LQR optimal feedback attitude controller to be computed on-the-fly for any given momentum wheel speed, system parameters, and state and input costs. Note that as $L \rightarrow 0$ the system decouples into three independent subsystems dependent on $(\phi_e, \omega_{e,x}^B)$, $(\theta_e, \omega_{e,y}^B)$, and $(\psi_e, \omega_{e,z}^B)$ as is usual for quadcopters.

C. Torque to Thrust Conversion

After the desired body torques $\boldsymbol{\tau}_u^B$ have been computed, the thrust forces required to achieve these torques while maintaining the total thrust commanded by the position controller are computed. Let $r_{i,x}$ and $r_{i,y}$ be the components of \mathbf{r}_i in the \mathbf{x}_B and \mathbf{y}_B directions. The equation below shows how the desired thrust force of each propeller is computed.

$$f_{P_i} = \frac{1}{4} \left(\begin{bmatrix} r_{i,y}^{-1} & -r_{i,x}^{-1} & \kappa_i^{-1} \end{bmatrix} \boldsymbol{\tau}_u^B + f_{cmd} \right) \quad (8)$$

The desired speed of each propeller can be computed based on the desired thrust forces as shown in [12]. Electronic speed controllers are then used to drive the propellers to their desired speeds.

IV. MOMENTUM WHEEL DESIGN

In this section we analyze the disturbance rejection properties of the linearized system and provide a framework for choosing the momentum wheel parameters.

A. Disturbance Sensitivity Analysis

The motivation for the addition of a source of angular momentum to the vehicle is based on the reduction of the state feedback \mathcal{H}_2 norm of the linearized system as the total angular momentum about \mathbf{z}_B is increased. We define the disturbance as $\boldsymbol{\tau}_v^B = (\tau_{v,x}^B, \tau_{v,y}^B, 0)$ and the output to be minimized as $z = C_1 x + D_{12} \boldsymbol{\tau}_v^B$, with C_1 and D_{12} defined based on Q and R in (6) so that $Q = C_1^T C_1$ and $R = D_{12}^T D_{12}$.

$$C_1 = \begin{bmatrix} Q^{1/2} \\ 0 \end{bmatrix}, \quad D_{12} = \begin{bmatrix} 0 \\ R^{1/2} \end{bmatrix} \quad (9)$$

In this context, the state feedback \mathcal{H}_2 norm can be considered the expected root-mean square value of the output z when the disturbances are unit variance, white noise torques about \mathbf{x}_B and \mathbf{y}_B [15]. Alternately, the state feedback \mathcal{H}_2 norm can be considered a sum of the signal energies of z for Dirac torque impulses about \mathbf{x}_B and \mathbf{y}_B [16]. The output

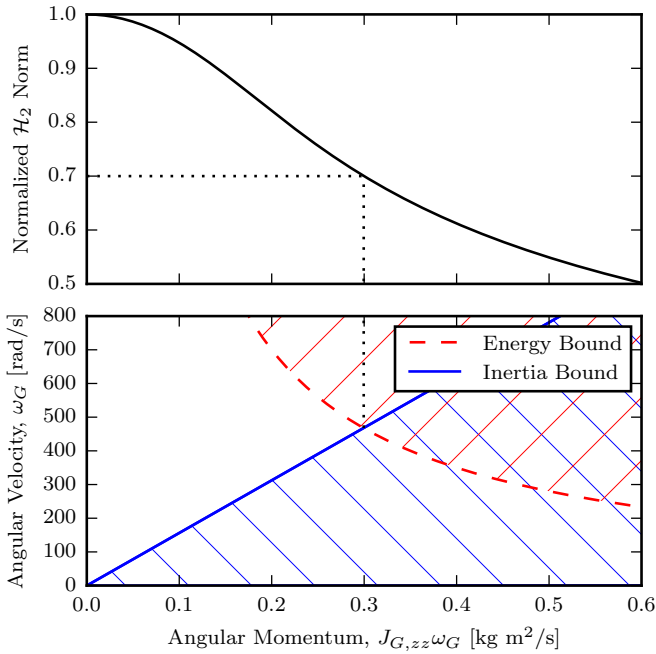


Fig. 4. Normalized \mathcal{H}_2 norm of linearized attitude dynamics (top) and range of feasible angular momentums (bottom). As the angular momentum of the momentum wheel increases, the system's sensitivity to disturbances (as quantified by the \mathcal{H}_2 norm) monotonically decreases. The maximum angular momentum of the wheel is bounded by constraints on the maximum moment of inertia of the wheel and by the maximum rotational energy allowed to be stored in the wheel. Both plots use parameters of the experimental platform.

signal energy is defined below. Note that the state feedback \mathcal{H}_2 optimal controller is equivalent to an infinite-time LQR optimal controller under full state feedback.

$$\begin{aligned} \|z\|_2 &= \left(\int_0^\infty z^T(t)z(t)dt \right)^{1/2} \\ &= \left(\int_0^\infty x^T Q x + (\tau_u^B)^T R \tau_u^B dt \right)^{1/2} \end{aligned} \quad (10)$$

Figure 4 shows how the normalized state feedback \mathcal{H}_2 norm of the system presented in (3) changes as the angular momentum of the momentum wheel increases. The state feedback \mathcal{H}_2 norm is calculated using the physical parameters of the experimental platform shown in Figure 1.

B. Choice of Momentum Wheel Parameters

As suggested by the state feedback \mathcal{H}_2 norm analysis, a design that maximizes the angular momentum of the momentum wheel is desired, but the size, mass, and speed of the wheel are limited by both physical and safety constraints. Although in theory the momentum wheel could spin as fast as the maximum speed of the motor driving it, this would result in a large amount of kinetic energy being stored in the wheel, which may pose a safety risk in the event of a crash or structural failure.

Thus, we choose to impose a bound on the maximum energy stored in the wheel, E_{max} , related to the maximum energy stored in the propellers of the vehicle. For the

experimental vehicle we choose E_{max} to be two times the maximum rotational energy stored in the propellers of the vehicle.

The mass moment of inertia of a single propeller used on the experimental vehicle was measured to be $1.9 \times 10^{-5} \text{ kg m}^2$, and the maximum angular velocity was measured to be 960 rad s^{-1} . The maximum rotational energy stored in the vehicle's propellers is then 35 J, giving $E_{max} = 70 \text{ J}$.

A second constraint on the total angular momentum is imposed by a limit on the mass moment of inertia of the wheel. This bound is based on the maximum allowed mass and size of the wheel, which is determined by the payload capacity and size of the quadcopter. Based on the payload capacity and size of the experimental vehicle, a maximum mass of 100 g and maximum radius of 9.5 cm were specified. The maximum inertia of an aluminum wheel designed to meet these constraints was found to be $J_{G,zz,max} = 6.4 \times 10^{-4} \text{ kg m}^2$.

An optimization problem for choosing the momentum wheel parameters is formulated below. The optimum angular momentum of the wheel occurs when $J_{G,zz}$ is maximized, and the optimum angular velocity of the wheel is determined by the maximum allowable energy.

$$\begin{aligned} \max_{J_{G,zz}, \omega_G} \quad & J_{G,zz}, \omega_G \\ \text{s.t.} \quad & \frac{1}{2} J_{G,zz} \omega_G^2 \leq E_{max} \\ & J_{G,zz} \leq J_{G,zz,max} \end{aligned} \quad (11)$$

A graphical representation of (11) is shown in Figure 4. The optimal rotational speed of the momentum wheel for the experimental vehicle is 468 rad s^{-1} , giving a maximum angular momentum of $0.30 \text{ kg m}^2 \text{ s}^{-1}$. This corresponds to a 30% reduction of the state feedback \mathcal{H}_2 norm of the system when compared to the same system without the wheel spinning.

V. EXPERIMENTAL RESULTS

This section presents the experimental results obtained from flights using the test vehicle shown in Figure 1. We first test the vehicle's ability to reject torque impulse disturbances, and then show the vehicle's reaction to a step change in desired hover position to demonstrate that the vehicle remains agile. Comparisons are made between vehicles with and without the wheel spinning.

A. Platform

A custom quadcopter and momentum wheel were used for testing. The physical parameters of the vehicle are listed in Table I. The position controller parameters were chosen to be $\zeta_p = 0.7$ and $\omega_p = 2 \text{ rad s}^{-1}$. The parameters for the Q and R matrices in (6) were chosen using Bryson's rule [17]. Specifically, we choose the following desired bounds on the states and inputs to the system, assuming $|r_{i,x}| = |r_{i,y}|$ by symmetry of the vehicle.

$$\begin{aligned} \phi_{max} &= \theta_{max} = \psi_{max} = 30^\circ = 0.52 \text{ rad} \\ \tau_{u,x,max}^B &= \tau_{u,y,max}^B = |r_{i,x}| f_{P_i,max} = 0.805 \text{ N m} \\ \tau_{u,z,max}^B &= |\kappa_i| f_{P_i,max} = 0.096 \text{ N m} \end{aligned} \quad (12)$$

TABLE I
TEST VEHICLE PHYSICAL PARAMETERS

Parameter	Value
m_B	822 g
m_G	100 g
$I_{B,xx}$	1.0×10^{-2} kg m ²
$I_{B,zz}$	5.5×10^{-3} kg m ²
$I_{G,xx}$	3.2×10^{-4} kg m ²
$I_{G,zz}$	6.4×10^{-4} kg m ²
$f_{P_i,max}$	6.86 N
$\ \mathbf{r}_i\ _2$	0.166 m
$ \kappa_i $	0.014 m

From the desired bounds on the states and inputs we select the parameters of the Q and R matrices as follows.

$$\begin{aligned}
 q_{xy} = q_z &= \frac{1}{(\phi_{max})^2} = 3.7 \text{ rad}^{-2} \\
 r_{xy} &= \frac{1}{(\tau_{u,x,max}^B)^2} = 1.54(\text{N m})^{-2} \\
 r_z &= \frac{1}{(\tau_{u,z,max}^B)^2} = 108.5(\text{N m})^{-2}
 \end{aligned} \tag{13}$$

The position and attitude of the quadcopter are measured directly by an external motion capture system, and the angular velocity of the quadcopter is measured using an onboard rate gyroscope. The position controller runs on an offboard computer and sends commands to the quadcopter via radio at 50Hz. The attitude controller is ran onboard the quadcopter at 500Hz.

B. Disturbance Rejection

The ability of the vehicle to reject torque disturbances was tested using a torque impulse created via a collision with a steel ball dropped from a height of 1 m above the hovering quadcopter. The quadcopter was modified to include an arm extension capable of withstanding a collision with the ball, and a second arm extension was included to balance the vehicle. The arm extensions had masses of 24 g each, slightly increasing the total mass and mass moment of inertia of the vehicle.

Two test cases were examined, both without the wheel spinning and with the wheel spinning at a speed of 468 rad s^{-1} . In test case (a), a ball with a mass of 67 g was used to generate a torque impulse of 0.092 N m s , and in test case (b) a ball with a mass of 135 g was used to generate a torque impulse of 0.186 N m s . The masses of the balls were chosen such that the collision with the smaller ball did not result in commanded thrust values higher than that maximum thrust $f_{P_i,max}$ for any propeller, while the collision with the larger ball did result in at least one propeller reaching the maximum thrust value during the test. The thrust produced by each propeller was additionally limited to be greater than 0 N.

Figures 5a and 5b show the position error, attitude error, and thrust range plots corresponding to test cases (a) and (b) respectively. Figure 6 displays a series of images showing how the quadcopter responds to test case (b).

C. Agility

The agility of the vehicle is demonstrated by commanding a step change in desired hover position. Figure 7 shows how each vehicle reacts to a 1.5 m horizontal step change in desired hover position. As shown, both vehicles perform similarly, indicating that the additional angular momentum provided by the momentum wheel does not seriously impede the agility of the vehicle.

D. Discussion of Results

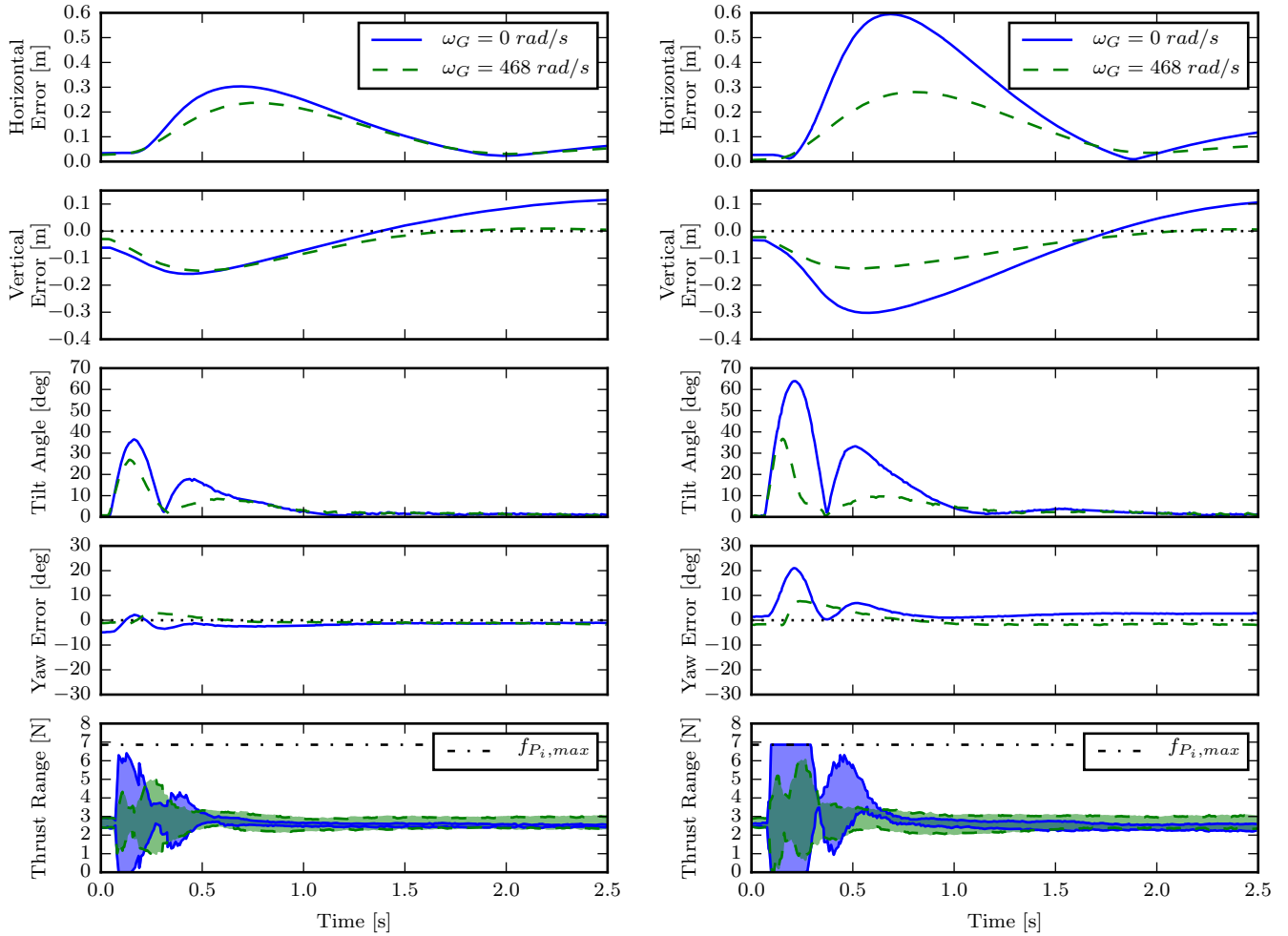
In order to verify the disturbance sensitivity analysis presented in Section IV-A, we compute the ratio δ of the output signal energy of the system for test case (a) with the stationary wheel (defined as z_1) and with the spinning wheel (defined as z_2). The ratio δ corresponds to the normalized state feedback \mathcal{H}_2 norm presented in Figure 4. In calculating the output signal energy we evaluate (10) numerically for $t \in [0, 2.5]$. The attitude component of the state vector x in (10) is computed using the Euler angles (ψ, θ, ϕ) as defined in Section II-B.

$$\delta = \frac{\|z_2\|_2}{\|z_1\|_2} = 0.68 \tag{14}$$

We observe an experimental reduction of the state feedback \mathcal{H}_2 norm by 32%, which only slightly differs from our predicted reduction of 30%. Although we have both theoretically and experimentally shown that the additional angular momentum provided by the momentum wheel can significantly improve the disturbance rejection of the vehicle, our analysis thus far has not included any constraints on the maximum thrust the propellers can produce, $f_{P_i,max}$. In test case (b), we observe that the disturbance is large enough to cause the thrust forces to reach this bound when the wheel is stationary. However, the thrust forces stay within their limits when the wheel is spinning. The lack of thrust saturation when the wheel is spinning results in position and attitude errors that are far lower than when the wheel is stationary. Additionally, we observe that the position and attitude responses are nearly identical for test cases (a) and (b) when the wheel is spinning.

The large difference in position and attitude errors observed in test case (b) implies that the use of a momentum wheel provides an especially large disturbance rejection improvement when the disturbances are large enough to cause the thrust forces of a standard quadcopter to saturate. The lack of thrust saturation implies that the vehicle with the spinning momentum wheel could reject even larger disturbances than the 0.186 N m s torque impulse without a significant increase in position and attitude error. Furthermore, these results suggest that vehicles carrying heavier payloads may expect to see a larger benefit from the added angular momentum due to their thrust forces being closer to saturation.

The step response of the vehicle to a change in desired horizontal position confirms that the vehicle retains the majority of its agility when the momentum wheel is spinning. This implies that a control strategy involving slowing the wheel before performing simple maneuvers is unnecessary.



(a) Collision with 67 g ball (0.092 N m s torque impulse)

(b) Collision with 135 g ball (0.186 N m s torque impulse)

Fig. 5. Responses to torque impulse caused by collision with steel ball dropped from 1 m. The tilt angle is defined as the angle between z_B^E and the vertical, and the thrust range is defined as the minimum range that contains all four thrust forces. When the wheel is stationary, the propeller thrust forces do not saturate after the 0.092 N m s torque impulse, but do saturate after the 0.186 N m s torque impulse. When the wheel is spinning, the propeller thrust forces do not saturate during either test. The thrust range at hover is slightly larger when the wheel is spinning due to drag forces acting on the wheel.

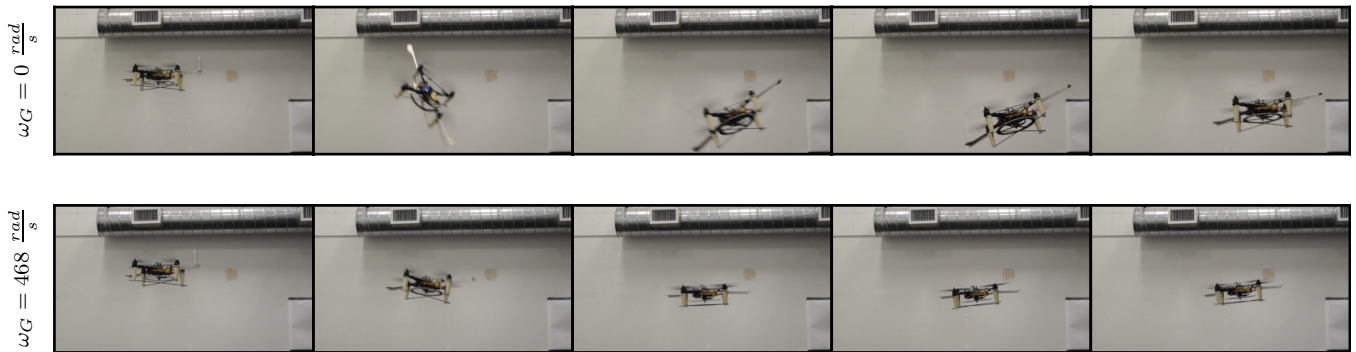


Fig. 6. Disturbance rejection with and without added angular momentum. The top series of images shows the quadcopter reacting to a mid-air collision with a 135 g ball (0.186 N m s torque impulse) without the momentum wheel spinning, and the bottom series of images shows the reaction when the momentum wheel is spinning at 468 rad s^{-1} . Images are spaced 0.2 seconds apart. A video of the experiments is attached to the paper.

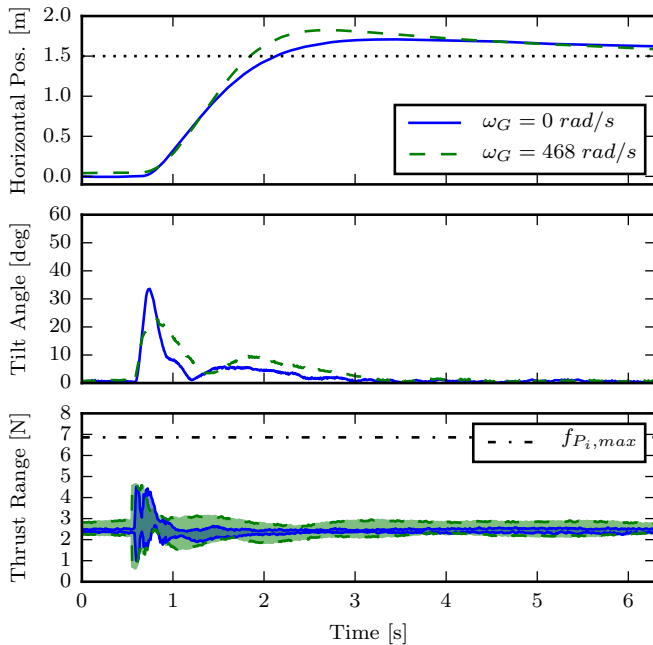


Fig. 7. Response to 1.5 m step change in desired hover position with and without the momentum wheel spinning. The additional angular momentum does not significantly affect the maneuverability of the vehicle.

An additional 11 W of mechanical power was required to lift the momentum wheel, and 4.7 W of mechanical power was required to spin the wheel at 468 rad s^{-1} , corresponding to a 27% increase in power consumption compared to a vehicle without the wheel. Note, however, that the experimental vehicle was not designed to optimize power consumption, meaning that a significantly lower power consumption could be attained by reducing the mass and drag forces acting on the wheel.

VI. CONCLUSIONS AND FUTURE WORK

In this paper we have derived the dynamics for a quadcopter with an added source of angular momentum, and have presented a suitable controller that includes an analytic solution for the LQR optimal attitude control gains. We have shown that the additional angular momentum can reduce the state feedback \mathcal{H}_2 norm of the linearized rotational dynamics, and have provided a method to choose the size and speed of the momentum wheel based on an energy bound approach. Furthermore, we have experimentally shown that the system can reject torque impulse disturbances better than a normal quadcopter while maintaining basic agility.

Because the propellers do not reach the maximum thrust limit as easily when the additional angular momentum is added, the augmented vehicle is especially useful in rejecting large magnitude torque disturbances. The ability of the augmented vehicle to reject large torque disturbances implies that it would be able to survive collisions that a standard quadcopter would not. Additionally, the effect of the momentum wheel on the vehicle's dynamics can be scaled by changing the angular velocity of the wheel, requiring no

additional mass to be added to the vehicle beyond the mass of the momentum wheel.

In future work we will investigate using the angular acceleration of the momentum wheel as an additional control input and analyze how the disturbance rejection capabilities of the vehicle scale with the size of the vehicle.

ACKNOWLEDGEMENT

This material is based upon work supported by the National Science Foundation Graduate Research Fellowship under Grant No. DGE 1752814 and the Powley Fund.

REFERENCES

- [1] A. Nishar, S. Richards, D. Breen, J. Robertson, and B. Breen, "Thermal infrared imaging of geothermal environments and by an unmanned aerial vehicle (UAV): A case study of the wairakei-tauhara geothermal field, taupo, new zealand," *Renewable Energy*, vol. 86, pp. 1256–1264, 2016.
- [2] S. Sharma, A. Muley, R. Singh, and A. Gehlot, "UAV for surveillance and environmental monitoring," *Indian Journal of Science and Technology*, vol. 9, no. 43, 2016.
- [3] I. Sa and P. Corke, "Vertical infrastructure inspection using a quadcopter and shared autonomy control," in *Field and Service Robotics*. Springer, 2014, pp. 219–232.
- [4] S. Waharte and N. Trigoni, "Supporting search and rescue operations with UAVs," in *2010 International Conference on Emerging Security Technologies (EST)*. IEEE, 2010, pp. 142–147.
- [5] K. Alexis, G. Nikolakopoulos, and A. Tzes, "Switching model predictive attitude control for a quadrotor helicopter subject to atmospheric disturbances," *Control Engineering Practice*, vol. 19, no. 10, pp. 1195–1207, 2011.
- [6] J. Bannwarth, Z. Chen, K. Stol, and B. MacDonald, "Disturbance accommodation control for wind rejection of a quadcopter," in *2016 International Conference on Unmanned Aircraft Systems (ICUAS)*. IEEE, 2016, pp. 695–701.
- [7] P. W. Likins, "Attitude stability criteria for dual spin spacecraft," *Journal of Spacecraft and Rockets*, vol. 4, no. 12, pp. 1638–1643, 1967.
- [8] M. Ryll, H. H. Bühlhoff, and P. R. Giordano, "First flight tests for a quadrotor UAV with tilting propellers," in *2013 IEEE International Conference on Robotics and Automation (ICRA)*. IEEE, 2013, pp. 295–302.
- [9] D. A. Wallace, "Dynamics and control of a quadrotor with active geometric morphing," Ph.D. dissertation, 2016.
- [10] W. Zhang, M. W. Mueller, and R. D'Andrea, "A controllable flying vehicle with a single moving part," in *2016 IEEE International Conference on Robotics and Automation (ICRA)*. IEEE, 2016, pp. 3275–3281.
- [11] M. W. Mueller and R. D'Andrea, "Relaxed hover solutions for multicopters: Application to algorithmic redundancy and novel vehicles," *The International Journal of Robotics Research*, vol. 35, no. 8, pp. 873–889, 2016.
- [12] P. Pounds, R. Mahony, P. Hynes, and J. M. Roberts, "Design of a four-rotor aerial robot," in *Proceedings of the 2002 Australasian Conference on Robotics and Automation (ACRA 2002)*. Australian Robotics & Automation Association, 2002, pp. 145–150.
- [13] P. H. Zipfel, *Modeling and Simulation of Aerospace Vehicle Dynamics*, 2nd ed. American Institute of Aeronautics and Astronautics, 2007.
- [14] B. Anderson and J. Moore, *Optimal Control: Linear Quadratic Methods*. Prentice-Hall International, 1989.
- [15] M. Green and D. Limebeer, *Linear Robust Control*. Dover Publications, 1995.
- [16] F. P. Geir E. Dullerud, *A Course in Robust Control Theory*. Springer, 2000.
- [17] A. Bryson and Y.-C. Ho, *Applied Optimal Control: Optimization, Estimation and Control*. CRC Press, 1975.